

Analysis of Chamber Simulations of Long Collecting Probes in High-Speed Dense Plasmas

Brian E. Gilchrist, *Member, IEEE*, Sven G. Bilén, *Member, IEEE*, Éric Choinière, *Student Member, IEEE*, Alec D. Gallimore, and Timothy B. Smith

Abstract—Chamber tests of simulated electrodynamic tethers (EDTs) of different geometries operating in a dense high-speed plasma are described. The geometries tested and described here are cylindrical and flat-ribbon tape. By moving the probe samples relative to the plasma source it was possible to vary the density and therefore the effective width over a range of approximately 1 to 2 Debye lengths (λ_D) for the cylinder sample and 6 to 19 λ_D for the tape samples. Several important conclusions can be drawn from the tests. 1) The current–voltage characteristics of the cylinder behave as predicted by orbital-motion-limited (OML) current collection theory in the saturation region. 2) The tape tether had comparable current levels to a theoretical equal area OML cylinder up to an effective width of at least $\sim 11\lambda_D$ and possibly wider. 3) Orienting the tape samples parallel or perpendicular to the plasma flow yielded different current responses (perpendicular is larger) above a bias potential that is near the estimated energy of the incoming beam ions. The observed difference was generally more pronounced at larger effective widths (higher densities). 4) It was also necessary to be above this bias potential to have a $V^{0.5}$ current–voltage character appropriate for an ideal cylinder in the OML regime. It is concluded that wide ribbon-like tape tethers can be effective current collectors but that velocity effects will be a factor to consider, especially as relative width of the tape tether (with respect to λ_D) grows.

Index Terms—Electrodynamic tethers, high-voltage sheath, Langmuir probes, orbital-motion-limited sheath, plasma current collection.

I. INTRODUCTION

IT HAS been predicted that operating in the orbital-motion-limited (OML) regime is especially beneficial for electron current collection to thin bare electrodynamic tethers (EDTs) with width dimensions on the order of a Debye length [1]. This configuration is different than that of Tethered Satellite System missions (TSS–1 and –1R), which used a large (with respect to

λ_D) spherical collector for electron collection [2]. The relative merits of bare tethers versus endbody electron collection is the subject of some debate [3]–[6]. However, it is likely that one or the other or a combination of both will be most appropriate for differing applications.

As part of NASA’s Advanced Space Transportation Program, the Propulsive Small Expendable Deployer System (ProSEDS) mission [11], which is to fly in 2003, will be the first to use the bare-tether concept and will demonstrate high current and measurable thrust; the technology is also being considered for other future missions. However, a small thin cylinder is not necessarily the best tether design when considering other practical factors such as tether lifetime. For example, to increase tether lifetime, one might consider a tether based on ribbon-like geometry (e.g., flat and wide) or more sparse structures involving interconnected conductor strands, and these tethers likely would have dimensions exceeding a Debye length. In low Earth orbit, dimensions of several centimeters or more could be needed to address micrometeoroid effects, which may represent several to more than 30 Debye lengths depending on plasma density [12]. These new geometries pose several questions that must be addressed before they can be employed. For example, how will the current collection performance change as a function of geometry and Debye length when compared to OML models or when in an ionospheric plasma moving at orbital velocities? Does the orientation of the ribbon with respect to the flowing plasma direction have an impact on collection efficiency?

This work describes two sets of vacuum chamber tests that simulated EDTs of different geometries operating in a dense, high-speed plasma. The geometries described here were cylindrical and flat-ribbon tape. The cylinder sample had a radius ranging 1 to 2 Debye lengths (as plasma parameters were varied), whereas the tape had a width that ranged from 6 to 19 Debye lengths. For these tests, the 6-m \times 9-m chamber operated by Michigan’s Plasmadynamics and Electric Propulsion Laboratory (PEPL) was used along with a PEPL/USAF-designed Hall thruster for the plasma source. These tests were done, in part, to support design efforts for future missions after ProSEDS.

II. OML CURRENT COLLECTION

In the OML regime, the electron current i , collected by a conductor in nonflowing plasma, is given by

$$i = n_e A_p q \frac{\sqrt{2}}{\pi} v_{te} \left(1 + \frac{qV}{kT_e} \right)^{0.5} \quad (1)$$

Manuscript received February 11, 2002; revised July 22, 2002. This work was performed under contract from The Michigan Technic Corporation and NASA-MSFC.

B. E. Gilchrist is with the Radiation Laboratory, Electrical Engineering and Computer Science Department, and the Space Physics Research Laboratory, AOSS Department, University of Michigan, Ann Arbor, MI 48109-2122 USA (e-mail: brian.gilchrst@umich.edu).

S. G. Bilén is with the Communications and Space Sciences Laboratory, Electrical Engineering Department, The Pennsylvania State University, University Park, PA 16802 USA (e-mail: sbilen@psu.edu).

É. Choinière is with the Radiation Laboratory, Electrical Engineering and Computer Science Department, University of Michigan, Ann Arbor, MI 48109-2122 USA (e-mail: echoinie@umich.edu).

A. D. Gallimore and T. B. Smith are with the Plasmadynamics and Electric Propulsion Laboratory, Aerospace Engineering Department, University of Michigan, Ann Arbor, MI 48109-2122 USA (e-mail: alec.gallimore@umich.edu; timsmith@umich.edu).

Digital Object Identifier 10.1109/TPS.2002.807538

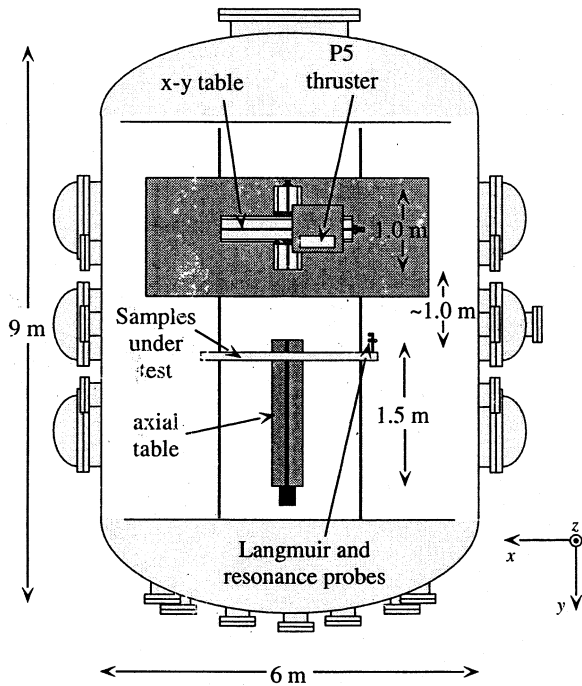


Fig. 1. PEPL LVTF as configured for tests.

where n_e is the electron number density in m^{-3} , T_e is the electron temperature (K), A_p is the probe area in m^2 , q is the electron charge magnitude, and k is Boltzmann's constant. V is the applied potential with respect to the plasma potential, i.e., $V = V_{\text{applied}} - V_{\text{plasma}}$. The thermal velocity here is given by $v_{te} = \sqrt{kT_e/m_e}$, where m_e is electron mass. For high potentials ($V \gg kT_e/q$), (1) reduces to

$$i = n_e A_p q \frac{\sqrt{2}}{\pi} \left(\frac{qV}{m_e} \right)^{0.5}. \quad (2)$$

We see that for large potentials, the current collected is independent of electron temperature and scales as the square root of the potential.

III. EXPERIMENTAL SETUP

A. Chamber Description and Setup

PEPL has as its centerpiece the Large Vacuum Test Facility (LVTF), a cylindrical stainless-steel-clad tank that is 9 m long and 6 m in diameter [14]. The facility has seven nude cryopumps backed by two 2000 cfm (56 600 l/s) blowers and four 400 cfm (11 300 l/s) mechanical pumps. These pumps give the facility a combined pumping speed of 500 000 l/s on air and 240 000 l/s on xenon and provide the ability to reach a high vacuum ($\sim 10^{-7}$ torr). Fig. 1 is a diagram of the LVTF as it was set up for these tests.

Two positioning tables were used to change the separation distance between the thruster and sample plane and to locate the sample under test directly along the thruster's centerline. The thruster was mounted on an x - y table that could move axially over a 1.0-m range and over a sufficient radial range to cover all samples. The samples were mounted on an aluminum frame that was connected to an axial table that could span a 1.5-m axial range (samples are described in more detail below). Combined

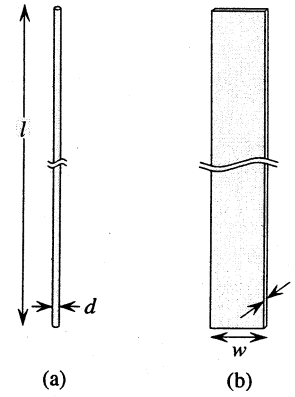


Fig. 2. Schematics of samples used for both test sets: (a) reference cylinder and (b) tape.

TABLE I
DESCRIPTIONS OF SAMPLES USED FOR BOTH TEST SETS

Sample	1	2	3
Description	Reference Cylinder	Perpendicular Tape	Parallel Tape
<i>first</i> length, l (cm)	10.0	9.4	9.2
<i>test</i> Width, w , or	0.28	1.9 (top) to	2.0 (top) to
<i>set</i> Diameter, d (mm)		2.1 (bottom)	2.2 (bottom)
<i>second</i> length, l (cm)	29.5	29.5	29.5
<i>test</i> Width, w , or	0.28	2.0 (top) to	2.0 (top) to
<i>set</i> Diameter, d (mm)		2.4 (bottom)	2.3 (bottom)

table movement allowed thruster-sample separation distance to change from ~ 1 to ~ 3 m. Changing separation distance was the primary mechanism for changing the plasma density seen at the sample plane.

B. Samples

Three different sample types are reported on here for use during these tests: cylindrical and flat-ribbon tape oriented parallel and perpendicular to the flow. Tungsten metal was used for all samples to ensure that they would endure the expected high temperatures that were caused by the collection of high-energy electrons to the samples' surfaces. During the first set of tests, the samples were approximately 10 cm in length, whereas during the second set of tests, they were approximately 30 cm in length. Two tape samples were used in both test sets, one where the width dimension was perpendicular to the plasma flow, the other with the width dimension parallel to the plasma flow. The thickness of the tape was $t = 0.1$ mm. Schematic representation of the samples is given in Fig. 2. Sample descriptions are summarized in Table I. Note that, due to the fabrication method, it was difficult to achieve width uniformity and exact matches in sample size for the tape samples. Table I documents this by indicating tape-width measurements at the sample tops and sample bottoms capturing the width nonuniformity. Total area differences between the samples are small, with the perpendicular tape having $\sim 2\%$ more area than the parallel tape in the first test set and the converse in the second test set.

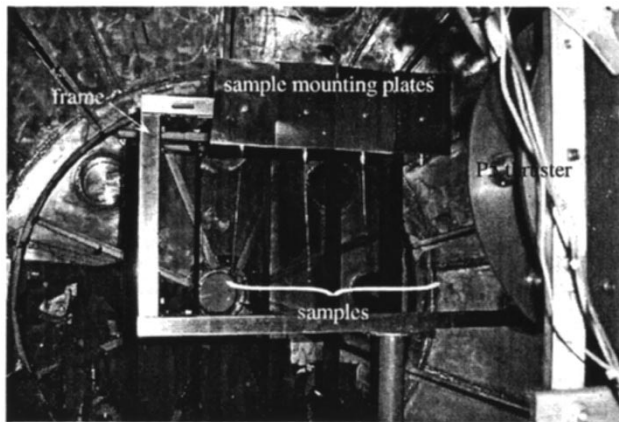


Fig. 3. Picture of the sample support structure for the second test set; structure for the first test set was very similar.



Fig. 4. P5 thruster.

All samples were soldered to the center conductor of a bulk-head safe high voltage (SHV) connector; the connector–sample interface was then covered with vacuum epoxy. This sample assembly was then mounted in a piece of stainless-steel flashing, which also functioned as the sample mounting plate. These mounting plates served as localized ground planes and were themselves electrically connected to the sample support frame. For both test sets there existed a minimum of 10-cm clearance between the samples and the frame. A picture of the setup is shown in Fig. 3.

Due to the energetic electron bombardment of the samples under high potentials, the samples would tend to heat up very quickly and probably exceed the melting temperature of most metals. Tungsten was, therefore, used for all samples because it has a melting temperature of 3695 K, which is significantly higher than other metals with low resistivity, such as copper, silver, or gold. Tungsten has a resistivity of $\rho = 5.51 \times 10^{-6} \Omega\cdot\text{cm}$, which is within a factor of 2–3 of these other metals.

By performing the following qualitative analysis, we can determine expected worst case temperatures for the tungsten during current collection. First, we assume the probe is thermally isolated, the surface is equipotential, and finally that all electrons collected at the surface (i.e., the electron current to the sample) have been accelerated to the potential of the sample. Then, the power heating the sample is simply $P(V) = I(V)V$, where V is the accelerating potential and the current I is a function of V . Fortunately, as the sample's temperature increases, so does its spectral emissivity, ε , which slows down runaway heating slightly. (The electron emission will also increase, but as we show below, for temperatures of our samples, this is negligible. For our estimate here, we assume $\varepsilon = 0.15$ and constant.) Using Stefan–Boltzmann's Law, we find the temperature T of the wire to be

$$T(V) = \left(\frac{P(V)}{\sigma A_p \varepsilon} \right)^{0.25} \quad (3)$$

where $\sigma = 5.6696 \times 10^{-8} \text{ W/m}^2\cdot\text{K}^4$ is the Stefan–Boltzmann constant and A_p is the surface area of the sample. From this equation, we see that T is a function of V . We also note that since P is linearly dependent on A_p in the OML collection

TABLE II
THRUSTER OPERATING PARAMETERS FOR BOTH TEST SETS

Parameter	First Test Set	Second Test Set
Chamber Pressure, Average (torr)	6.5×10^{-6}	4.9×10^{-6}
Discharge Voltage, V_d (V)	100	100
Discharge Current, I_d (A)	5.3	4
Inner Magnet Current, I_{im} (A)	2.99	1.04
Outer Magnet Current, I_{om} (A)	1.99	1.03
Cathode Voltage, V_c (V)	−19.7	−19.2
Heater Voltage, V_{htr} (V)	7.1	6.0
Anode Flowrate, \dot{m}_a (sccm)	60	45
Cathode Flowrate, \dot{m}_c (sccm)	6	6

regime and A_p is found in the denominator of the right-hand side of (3), surface area drops out of the equation. This means that neither increasing nor reducing the surface area will alleviate heating issues. Calculations show that at potentials above ~ 300 – 400 V for the plasma densities of these tests, the tungsten is in danger of melting. Hence, a second temperature mitigation method is needed if potentials higher than these values are used. By pulsing voltages at a low duty cycle, the sample is given a chance to cool off before the next pulse of high voltage heats it. The on-time must be short because the heating occurs quickly, on the order of tens of milliseconds.

The possibility of thermionic emission due to wire heating has been considered. At the highest applied voltages and positions closest to the thruster, the tungsten samples would briefly glow an orange-yellow color, indicating a temperature in the 2000 K range. Maximum possible thermionic emission currents from tungsten can be estimated from the Richardson–Dushman emission equation for a clean metal surface [15]. Even at these temperatures, electron emission currents fall below 1 mA/cm^2 , which is $<2\%$ of the collected current. Indeed, the use of tungsten as emitters has the disadvantage that it must be heated to very high temperatures in order to emit significant levels of current [15].

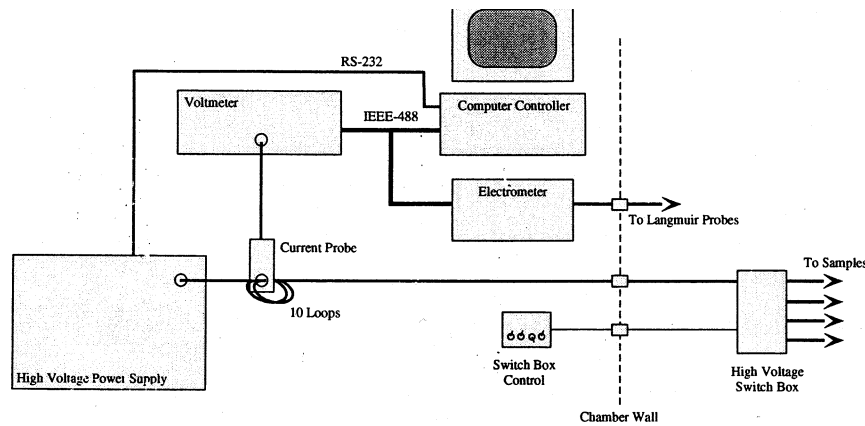


Fig. 5. Schematic of the test equipment setup.

C. Thruster Description and Operating Conditions

The PEPL/AFRL “P5” 5-kW-class Hall-effect thruster was used to provide a flowing plasma for these experiments. A detailed description of the P5 thruster is given by Haas *et al.* [16] and a picture of this thruster is shown in Fig. 4. When operating nominally, the P5 plasma is too fast and dense for the conditions that were needed; hence, for these tests the thruster was set at off-nominal conditions in order to lower the plasma velocity and density seen along the thruster’s axial direction. The P5 operating conditions for both sets of tests are given in Table II.

At the time of the tests, the emitted beam energy could only be estimated (~ 20 – 50 eV assuming a 100-V discharge voltage) since the discharge voltage was below the nominal thruster operating range and sensors were not available to help resolve the character of the P5 flow. Recently, additional tests using laser-induced fluorescence (LIF) measurements have allowed us to better estimate bulk and near-field ion beam velocity for the Table II conditions.

The LIF measurements used an argon-ion pumped Coherent dye laser system (model 899-29) to characterize the near-field plume plasma of the P5 Hall thruster. This ring dye laser is capable of outputting a continuous single-frequency beam on the order of 0.1 to 1.0 W with a line width of 1 MHz from 375 nm (near UV) to 900 nm (near IR). The laser system, operated at the 605.1-nm absorption line of singly ionized xenon, was used to perform plume diagnostics (velocimetry, relative density, temperature measurements, etc.) on the P5 Hall thruster. The measurements were based on a three-beam multiplex configuration, pioneered by Keefer [18] and expanded by Williams [19], [20], which yields simultaneous azimuthal, axial, and radial velocity components.

The LIF measurements were taken at a distance of 63 cm from the thruster, which, as will be seen, is closer than the zone for the simulated tether measurements. However, because the momentum transfer collision mean-free path was on the order of several tens of meters, these LIF measurements are believed to be representative of our experimental zone near the central axis. The results indicate that the total beam energy values along the thruster’s boresight were approximately 37 and 45 eV for Test-1 and Test-2 power settings, respectively. An experimental error of several electronvolts is estimated.

D. Data Collection and Measurement System

1) *Current–Voltage Measurement System:* A schematic of the current–voltage measurement system is given in Fig. 5. The system consisted of a Universal Voltronics BRC 20 000 HV power supply connected to the tether samples by way of a switch box inside the chamber. The HV power supply was controlled via RS-232 by the computer controller running a custom virtual instrument (VI) under LabVIEW. The computer commanded the HV supply to a specified voltage and then quickly back to zero (within 50–100 ms) to minimize sample heating. Before returning to zero, the supply’s internal voltage sensor reported back the actual voltage obtained. We verified that the supply pulses were long enough such that the voltage had reached a steady-state value. An American Aerospace Controls 835-2-10 current sensor (ammeter) was used to measure current. To increase sensitivity, the HV supply line was looped through the sensor ten times. Since the output of the ammeter was a voltage signal, an HP 34401A voltmeter was used to measure it and, in conjunction with the voltage measurement described above, these values were recorded as voltage–current pairs.

2) *Plasma Parameter Measurements:* Vertically oriented (perpendicular to the flow) Langmuir probes (LP) were used to measure the plasma environment. The LP sweeps were made by a Keithley 2410 source electrometer and collected via a custom LabVIEW script using a computer controller (Fig. 5).

A pressure map of the LVTF was generated after the tether experiments [21] and it was determined that the true xenon pumping speed with four pumps (the configuration used in these tests) is 140 000 l/s. This map was created by using a rake of five calibrated ion gauges that was swept through approximately 35% of the vacuum chamber (assuming symmetry this accounts for 70% of the tank or the entire thruster plume region of the engine). The thruster (cold flow) was operated at a number of mass flow rates and more than 800 points were collected in the pressure mapping measurements and, along with associated particle-in-cell modeling, is reported in [21]. Thus, a good understanding of the average chamber pressure present for the tether tests is available.

Using the chamber pressure values and recently measured charge exchange collision cross sections [22], [23] with an average ion beam energy of 45 eV for both test cases, various

TABLE III
MFPS AND ION BEAM SURVIVAL PERCENTAGES

Collision	First Test Set	Second Test Set
	6.5×10^{-6} torr	4.9×10^{-6} torr
Chamber Mean Free Path (m)		
XeII + XeI Charge Exchange	6.5	8.6
XeIII + XeI Charge Exchange	13.0	17.3
Ion–Neutral Elastic	80.9	77.4
Beam Survival Percentages		
Beam Survival at 0.75 m	90%	92%
Beam Survival at 1.0 m	86%	90%
Beam Survival at 3.0 m	65%	72%

mean-free path (MFP) lengths were calculated and are shown in Table III. The calculations assumed that 10% of the beam is composed of Xe^{++} and the rest is singly ionized xenon. It is believed this is conservative given the fact that the P5 was operated at only 100-V discharge potential and hence would not be expected to have too many multiply charged ions. As can be seen in Table III, the single ion-neutral charge exchange ($\text{XeII} + \text{XeI}$) MFPS are approximately 6.5 and 8.6 m for test cases 1 and 2, respectively, while the respective double ion-neutral ($\text{XeIII} + \text{XeI}$) MFPS are between 13 and 17 m for both cases.

By applying Beer's Law to find the ion beam survival rate (taking into account the weighting of the $\text{Xe}^+/\text{Xe}^{++}$ beam fraction), it is found that some 90% or more of the beam ions reach the tether samples 1 m from the thruster for both cases. At the far axial point of interrogation (3 m), far less than half of the beam ions have been lost to charge exchange. The low-energy charge exchange ions are free to diffuse throughout the $6\text{-m} \times 9\text{-m}$ volume of the vacuum chamber and essentially create a low-density plasma through which the beam ions flow. While it is difficult to directly estimate the background density that should result from the charge exchange ion production, if it is assumed that the charge exchange plasma is produced in a 6-m long by 30-cm diameter cylinder along the beam axis and is free to diffuse throughout the chamber volume, the plasma density should be well below 1% of the beam density. Thus, it is believed that a large majority of the particles that reach the tether samples—even 3 m from the thruster—are beam ions.

IV. DATA

In order to better understand the data presented here, we present first the plasma environment for both test sets and then the data collected during those tests.

A. Plasma Environment

Fig. 6 reports the measured plasma density and temperature as a function of distance for both test sets. By positioning the sample plane closer and farther from the thruster, we were able to obtain approximately a factor-of-10 change in plasma density. The density values shown here were extracted from the electron saturation regime of data collected by our vertically

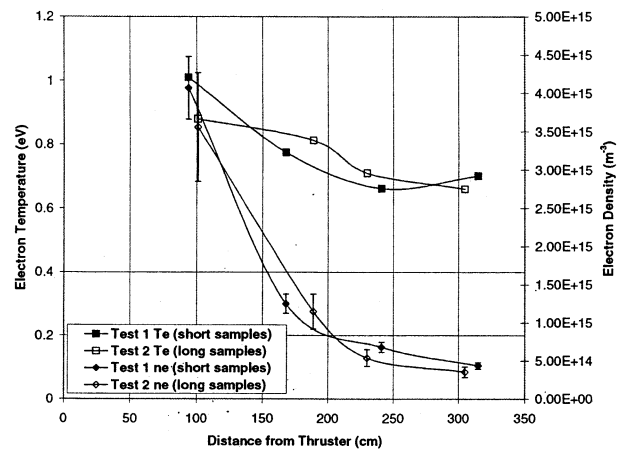


Fig. 6. Plasma parameters measured for both test sets.

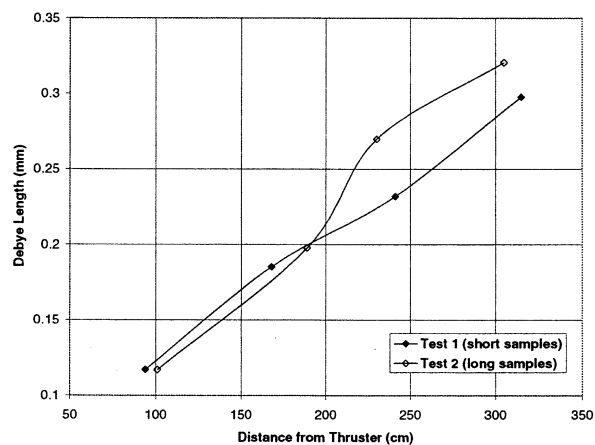


Fig. 7. Debye lengths derived for both test sets.

oriented reference cylinder probe, where the data is seen to saturate according to OML theory, i.e., we observe a linear relation between the square of current (I^2) and voltage (see Figs. 10 and 11).

The high-speed directional flow of the plasma is believed to be responsible for the observed delay in the current saturation (saturation occurred in the 75–100 V range on the reference cylinder). Langmuir probe sweeps were also performed over a smaller range ($-21 \text{ V} \leq V \leq +21 \text{ V}$) with the intent of determining the plasma parameters independently. However, the swept voltage range was insufficient to achieve current saturation and it was therefore decided to use the electron saturation data from the reference cylinder to determine the electron density. The electron temperatures shown in Fig. 6 were determined using the electron retardation regime data from the Langmuir probe sweeps. In addition, we were able to establish that over at least a $\pm 15\text{-cm}$ radial distance from the central axis there is less than 10% variation in plasma density.

Fig. 7 shows the calculated Debye lengths for both test sets ($\lambda_D = \sqrt{\epsilon_0 k T_e / q^2 n_e}$). The cylindrical sample had a radius $r = d/2 = 0.14 \text{ mm}$, so we can see from the Debye lengths obtained that the cylinder's diameter spanned a range of $\sim 1\text{--}2\lambda_D$. The tape width of $\sim 2\text{--}2.4 \text{ mm}$ represents from 6 to 19 times the Debye length. This ability to span from scalelengths on the order of λ_D up to many times λ_D allows us to examine the limits

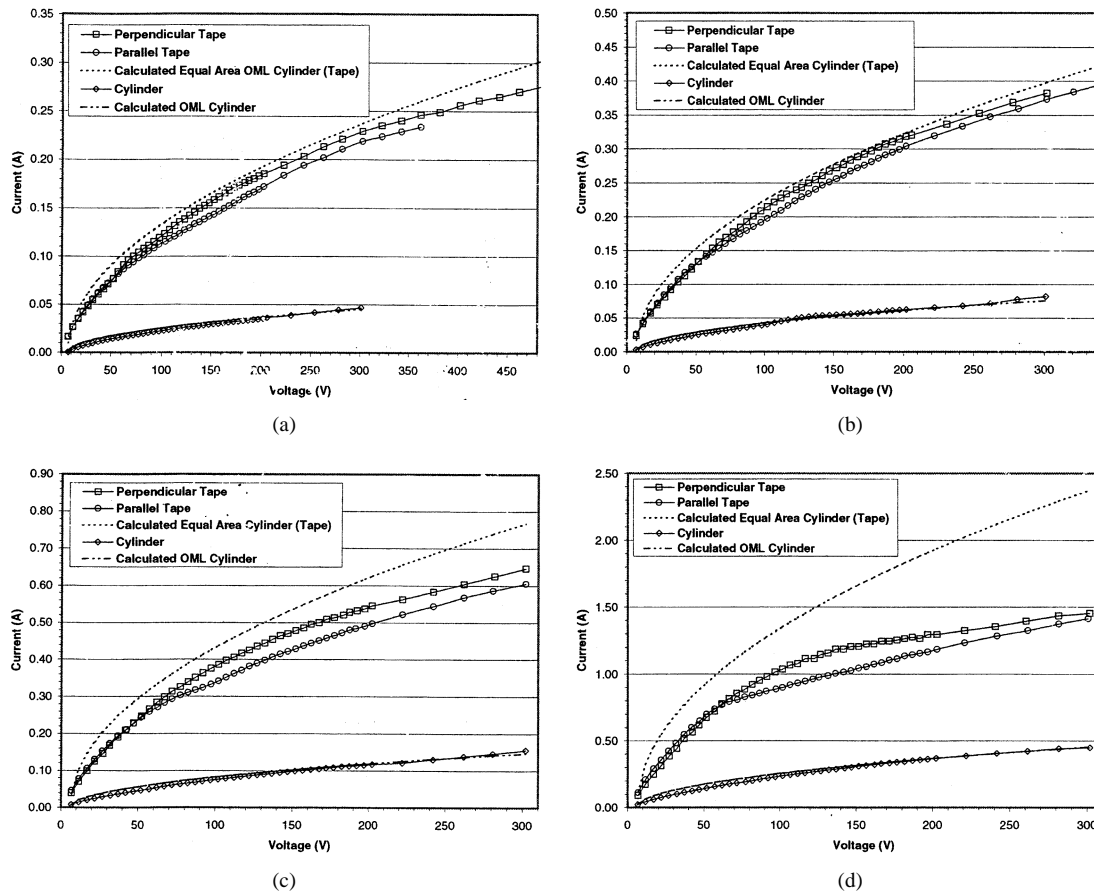


Fig. 8. Current as a function of voltage for the tape and cylinder geometries from the second test set at separation distances of (a) 305 cm, (b) 230 cm, (c) 187 cm, and (d) 100 cm.

of the OML model of current collection and provides data complementary to that reported in [17].

B. Current Collection Data

The first data figure (Fig. 8) plots the current as a function of voltage for the tape and cylinder geometries from the second test set (Test 2) at separation distances of 305, 230, 187, and 100 cm, respectively, which represent lower to higher plasma densities (see Fig. 6). Note that the zero potential reference point in these plots is chamber ground, which means that the plasma potential has not been removed. They also include two cylindrical OML-current-model curves for comparison purposes to answer roughly what would be the expected OML response as described in (1) for a small probe in a stationary plasma. For the reference cylinder, (1) has been “fitted” to the data using a 7-V plasma potential (close to the measured plasma potential using the Langmuir probe), the reference cylinder radius of 0.14 mm, and a plasma density value that optimized the fit to the reference cylinder data. Using this fitting process, the resulting density values for all probe distances are within 5% of the values given in Fig. 6. Using these “derived” values, which allows more straightforward comparison of collected currents, a second cylindrical-OML response curve is plotted using a cylinder perimeter equal to the tape perimeter (this resulted in an equal area cylinder radius of ≈ 0.73 mm). In general, this second OML response for the tape samples is near the experimental data at the furthest two separation distances, but overpredicts the experimental data at the two shortest distances where the effective

tape width is larger in terms of λ_D . It is also noted that at all distances and for both the reference cylinder and tape samples, the OML-curve predictions rise more rapidly than the experimental data at the lower potentials. Finally, it is noted that the parallel and perpendicular tape orientation data deviate from each other at a potential near a 50-V bias.

Fig. 9 duplicates the information in Fig. 8 for Test 1 at distances of 315, 241, 168, and 94 cm. The equation(1) fit to the reference cylinder uses a 7.5-V plasma potential and density values that are within 4% of the Fig. 6 values. The equal-area-cylinder OML plot used to compare with the tape probes had a radius of 0.67 mm, which was appropriate for the parallel tape probe. The perpendicular probe area is approximately 2.7% smaller. In general, the equal-area OML cylinder agrees with the tape data at the three farthest distances. The 94-cm tape response appears close but could be starting to underperform the OML prediction. A rather sharp deviation in the parallel tape response is seen in the 315-cm data [Fig. 9(a)] near 220 V and a similar, but slower, shift is seen in the perpendicular data around 300 V. We have no clear explanation for this shift. The deviation between parallel and perpendicular data seen clearly in the Test 2 data (Fig. 8) is less obvious in the Test 1 data except for the closest distance [Fig. 9(d)].

The Test 2 and 1 measured data (Figs. 8 and 9, respectively) have also been plotted again as I^2 versus V in Figs. 10 and 11 along with best fit straight lines in the linear regions of each dataset. In each case, the best fit to the slope was obtained by first using the Fig. 6 plasma density data and then adjusting the

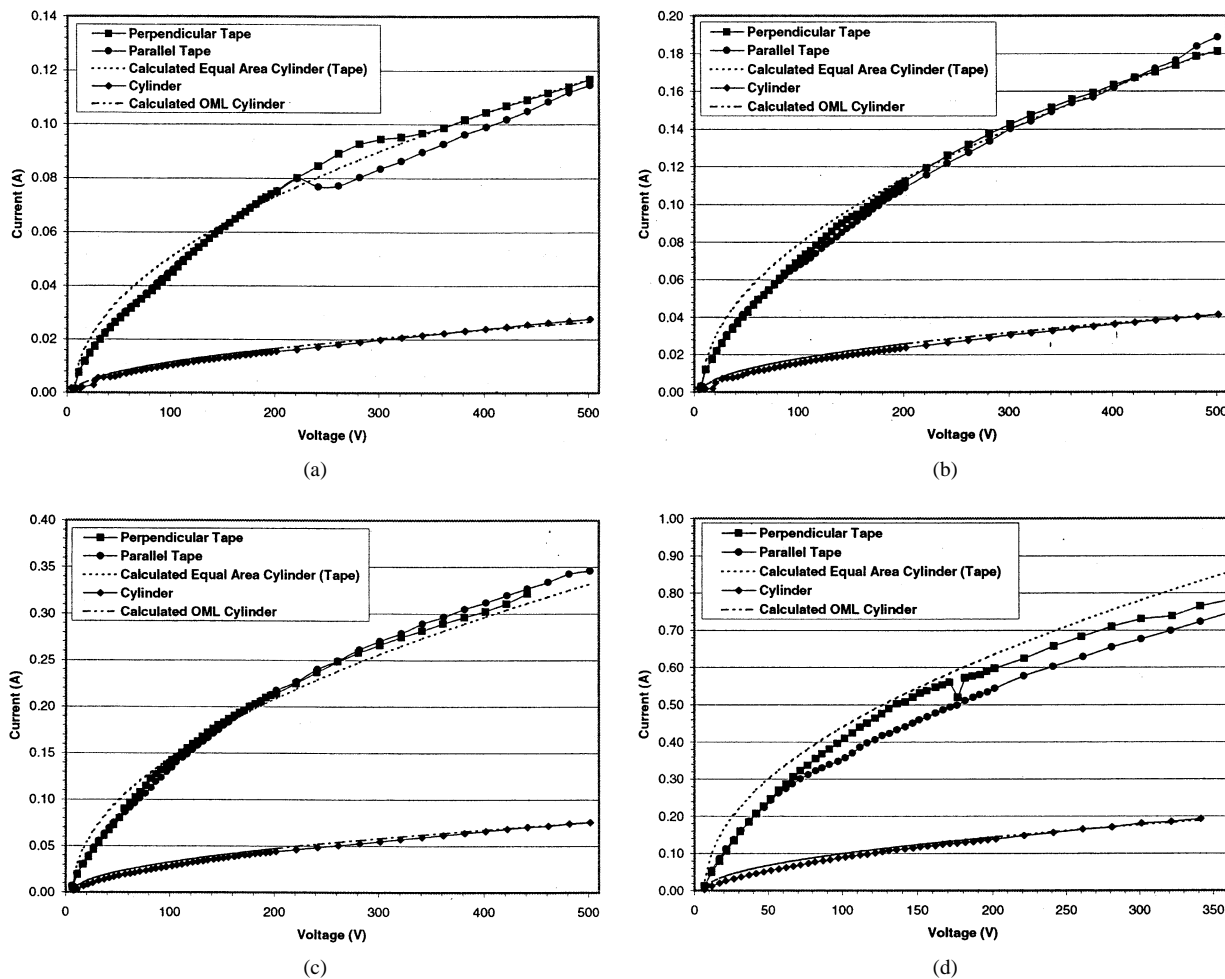


Fig. 9. Current as a function of voltage for the tape and cylinder geometries from the first test set at separation distances of (a) 315 cm, (b) 241 cm, (c) 168 cm, and (d) 94 cm.

total collection area (same as adjusting the perimeter or effective radius for a common probe length). An area efficiency factor is quoted in the plot legend for each curve that shows a similar reduction in effectiveness as suggested from Figs. 8 and 9.

Figs. 10 and 11 are useful to illustrate the region where the $V^{0.5}$ behavior is achieved for each data set. It is noted that for the farthest distance perpendicular tape measurement of Test 2 [Fig. 10(a)] and for the three farthest distances of Test 1 [Fig. 11(a)–(c)], the applied voltage bias was allowed to increase up to 500 V. The tape samples in all of these cases are observed to have the current response fall below a $V^{0.5}$ behavior above 225 V in one case and above the 275- to 300-V range in the others. On the other hand, the reference cylinder cases showed a current response that slowly went above a $V^{0.5}$ behavior for potentials greater than 250 to 300 V in both Tests 1 and 2. In all but the 100-cm case for Test 2, the difference in current between the orientations at the higher potentials remained roughly constant. The 100- and 94-cm cases appear to show the two curves converging as can be seen in either Fig. 8(d) or 10(d).

Fig. 12 provides a method of directly comparing the differences between Tests 1 and 2 given the approximately factor-of-three difference in sample lengths and small differences in perimeters. In Fig. 12, before plotting, the currents obtained in Test 1 were multiplied by an area-scaling factor

using the measurements in Table I and a plasma density-scaling factor using Fig. 6. All else being equal, the two datasets should agree. As seen in the figure, the cylinder samples indeed are approximately the same at all distances. However, Fig. 12(a), (c), and (d) all show the scaled Test 1 currents separating from the Test 2 currents near the 50-V bias point but generally tracking each other below this point (suggesting the area and density scaling factors are appropriate in at least these situations). While Fig. 12(b) at first does not appear to follow the same trend, we suspect that there is experimental error that we cannot identify that is causing the Test 1 scaled currents (reference cylinder and tape samples) to be reported about 14% low. If the Test 1 currents were increased by this 14% factor, Fig. 12(b) would show the same character as the other distances. The implication of the character seen in Fig. 12 is discussed in the next section below.

V. OBSERVATIONS AND ANALYSIS

There are several interesting and intriguing observations that result from the data collected during the tests presented above. From Figs. 8 and 9 it can be seen that the perpendicular orientation consistently exceeded the collected current of the parallel orientation above a certain potential, even when accounting for the approximately 2% difference in surface areas of the perpendicular and parallel orientations in both Tests 1 and 2. In

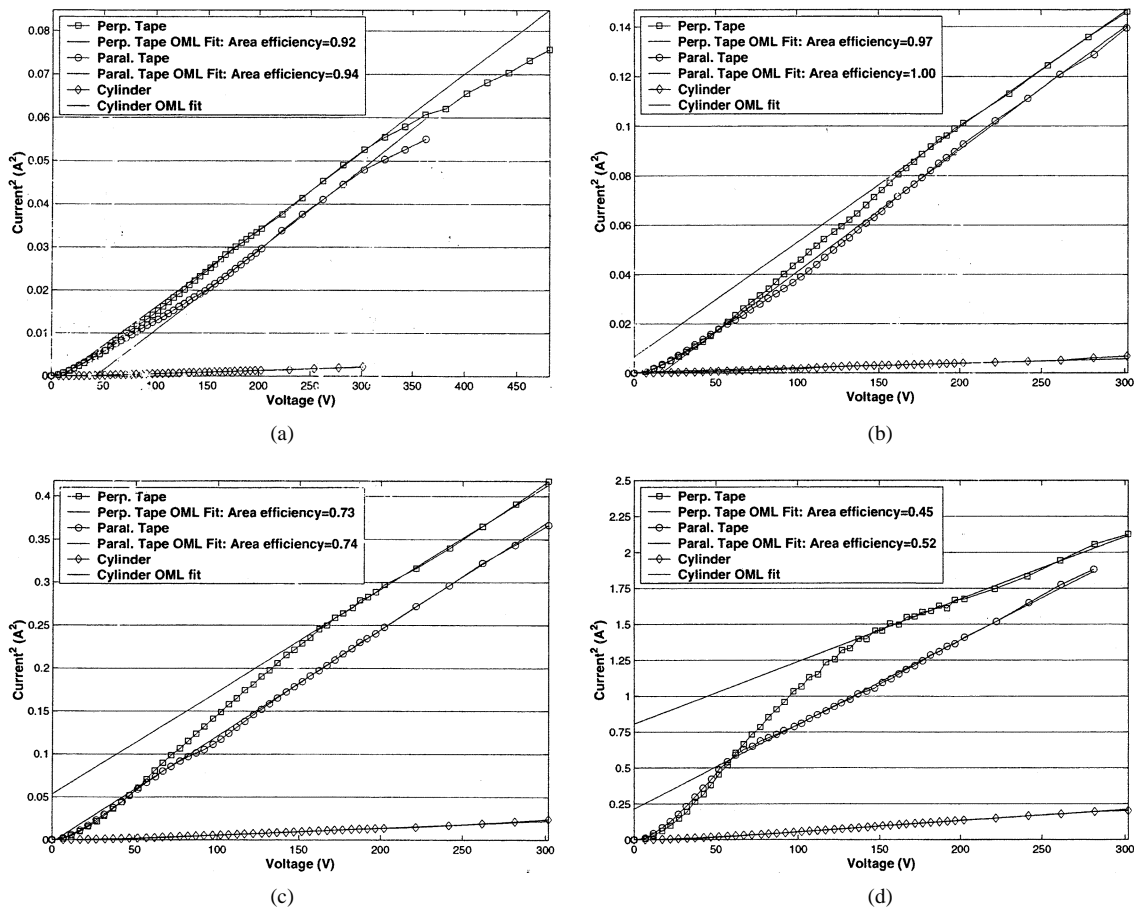


Fig. 10. "Current squared" as a function of voltage for the tape and cylinder geometries from the second test set at separation distances of (a) 305 cm, (b) 230 cm, (c) 187 cm, and (d) 100 cm.

all cases, the onset of the separation between curves for the different orientations occurred near a threshold of 50-V bias and thus must be independent of plasma density as well as current magnitude. We believe this effect must be attributed to the plasma motion.

Similarly, the fact that a $V^{0.5}$ character is not achieved until a high bias point may also be attributed to the motion of the plasma and the energy of the ion beam (37 and 45 eV for Tests 1 and 2, respectively). Probe orientation also appears important. We conclude this by inspection of Figs. 8 and 10 for Test 2, which suggest that as the samples were moved to closer distances, it is the parallel orientation that first has a "knee" in the $I-V$ curve and begins following a $V^{0.5}$ slope (this is less obvious at the furthest distance). Then, at a higher bias potential, in the 150- to 200-V range, the perpendicular sample changes its slope to begin following the $V^{0.5}$ response. For Test 1 (Figs. 9 and 11) a similar character is less obvious until reaching the closest distance.

It is interesting to note that a change in current collection behavior beyond a certain bias threshold was also seen in the TSS-1R [24] and TSS-1 missions [25] where the threshold was at a potential of the ionospheric ion ram kinetic energy. Specifically, the TSS-1R results found that as the satellite potential exceeded the ram kinetic energy of O^+ ions (5.3 eV), the level of kilohertz wave activity increased dramatically [26] and a suprathermal electron population appeared at the satellite's surface [27]. The distributions of wave activity and suprathermal

electron fluxes were quite nonuniform around the satellite, indicative of both ram and magnetic field limitations to the current collection. These results were also in qualitative agreement with previously reported results from the TSS-1 mission [28], but extend over a substantially larger range of currents and satellite potentials. We note that the knee in our case for the parallel orientations, occurring near 50 V in Fig. 8, is very close to the estimate of 45-eV ion beam energy determined via LIF measurements for Test 2, especially when the plasma potential correction is applied. Additional measurements will be required to determine what effects are causing the knee in our response independent of plasma density.

Regardless of possible plasma-motion-induced effects, we wish to understand how well present OML models of cylindrical probes predict the responses we observed for our tape samples (e.g., current collection capability). Sanmartín and Estes [30], [31] have considered tape geometries in the OML regime of a stationary, unmagnetized plasma and concluded that there are dimensions beyond a Debye length, depending on plasma parameters, where a thin tape could still satisfy OML collection. They define an equivalent radius R_{eq} for the tape that depends on both cross-section perimeter and shape and on dimensionless parameters in the plasma that they use to compare with a maximum allowed radius, R_{max} , for OML validity ($R_{eq} \leq R_{max}$). For the tape samples here, $R_{eq} \sim \text{perimeter}/8 \sim 0.58$ mm. Their conclusions for the case appropriate to our experiments ($T_e \sim T_i$) would suggest

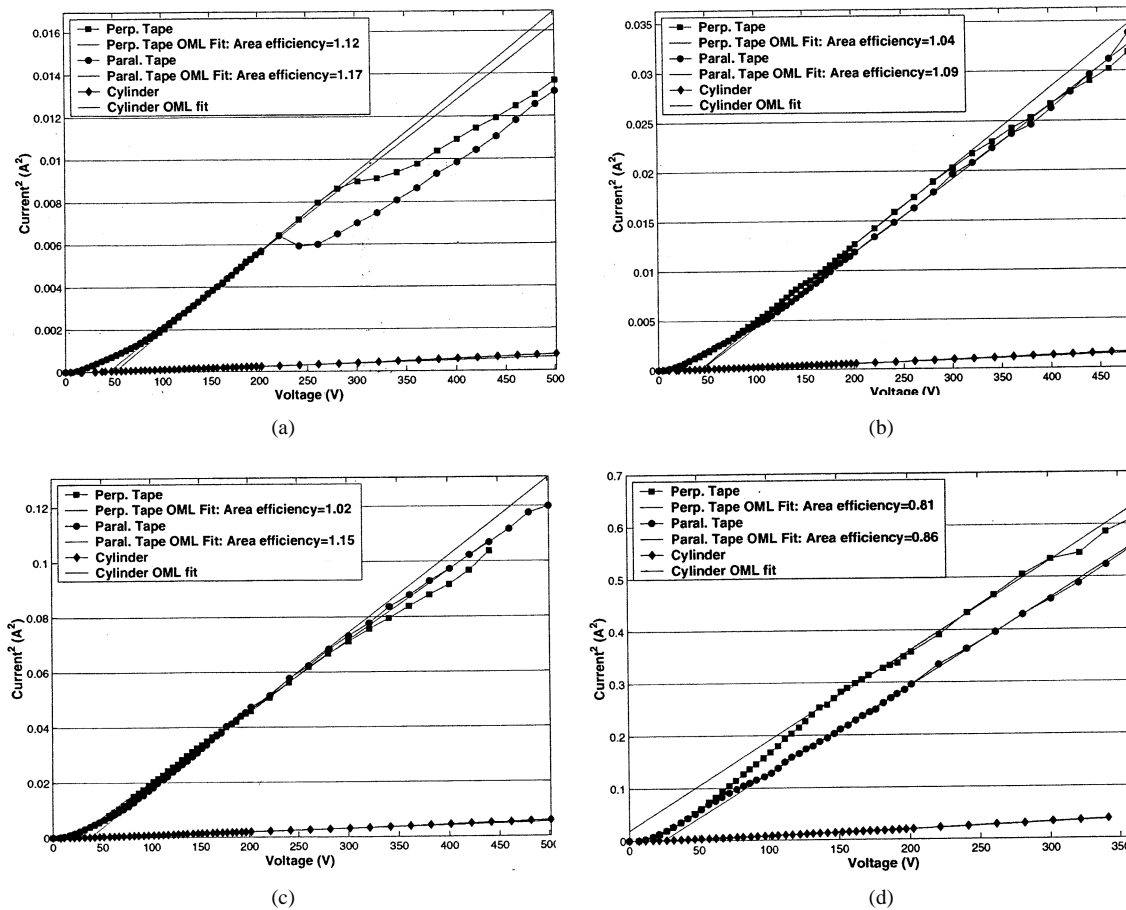


Fig. 11. “Current squared” as a function of voltage for the tape and cylinder geometries from the first test set at separation distances of (a) 315 cm, (b) 241 cm, (c) 168 cm, and (d) 94cm.

that $R_{\max} \sim \lambda_D$ and, based on Fig. 7 estimates for Debye length, we should underperform at all distances. Note that in Fig. 8 an equal-area criterion for the effective radius (0.73 mm) was used for the OML plots to compare with the tape data. If the smaller value of 0.58 mm were used, these OML curves for the tape comparison would be scaled by a factor of 0.79 and it would be concluded that the tape responses for Fig. 8(a) and (b) were somewhat enhanced, approximately in agreement for Fig. 8(c), and still underperforming for Fig. 8(d) relative to OML theory using R_{eq} as defined by Sanmartín and Estes. A similar assessment for Test 1 results shown in Fig. 9 would conclude that at all distances the actual response exceeded the OML prediction.

It may also be of practical benefit to compare our results directly with tape width given that the samples are thin. Using Fig. 7, the effective widths of the test samples in Test 2 were approximately 6.9, 8.1, 11.1, and 18.8 Debye lengths for the farthest to nearest distances, respectively. Assuming negligible thickness for the tape samples, Sanmartín and Estes [30], [31] would indicate that OML response could be maintained out to a tape width of approximately $4\lambda_D$. Recently reported experimental work using probes up to a few λ_D width by Kruijff *et al.* [17], [29] suggest OML is still valid up to the maximum dimension they tested. In the tests presented here, we have significantly exceeded this dimension. By inspection of Fig. 8 and using the 0.79 scaling factor described above it would appear that somewhere above $11\lambda_D$ but below $19\lambda_D$ tape width, the actual response begins to underperform an

OML response. (This limit would be only slightly smaller if the equal-area OML cylinder model were used instead as in Fig. 8.) A similar analysis using Test 1 data in Fig. 9 suggests that the OML model holds even further out to at least near $19\lambda_D$. A more recent paper by Estes and Sanmartín [32] suggests that their threshold prediction may be weak, i.e., degradation in performance is not rapid beyond the theoretical limits. This certainly appears to be the case here.

Whether or not the experiments demonstrate that a size limit for OML validity has been reached in the moving plasma is open to interpretation. The OML character could be affected by probe size or shape, the moving mesosonic plasma around the probes, and/or experimental limitations. With regard to the latter, we have considered two possible issues: current source limitations of the thruster and probe “end-effects.” Current limitations may be a concern if the collected current level exceeds what can be drawn from the plasma source without altering the environment around the probe. In general, 80% of the discharge current is estimated to be available to the emitted plasma beam, which would be 4.2 and 3.2 A for Tests 1 and 2, respectively. In Test 2 [Fig. 8(d)], up to 1.4 A was collected to the probe, which is a significant fraction (44%) of the available current emitted by the plasma source. Inspection of Fig. 12 shows that the reference cylinders agreed well at all distances. In particular, the closest distance [Fig. 12(d)] suggests that currents up to 500 mA are certainly available from the plasma source without affecting the plasma environment. If this is true, then the separations between Test 1 and 2 results in Fig. 12(a) and (c) [and a “corrected”

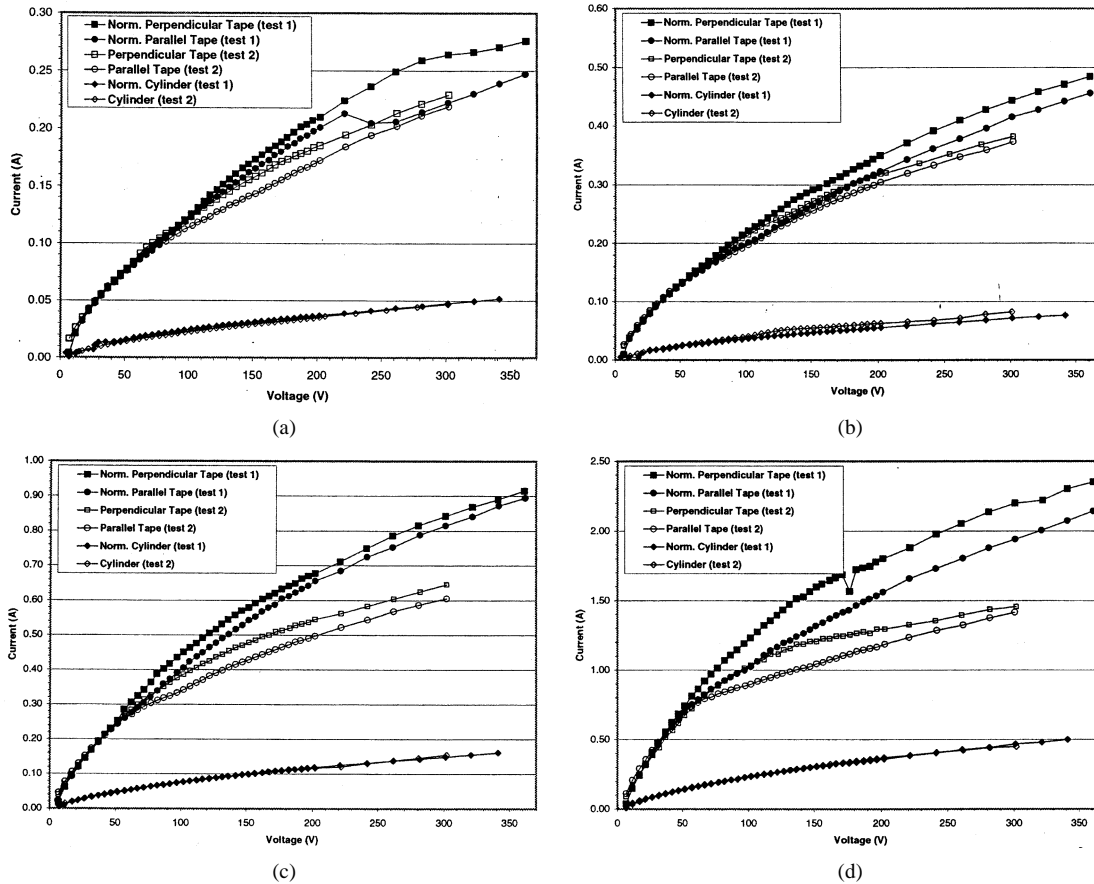


Fig. 12. Comparison of Tests 1 and 2 at separation distances, respectively, of (a) 315 and 305 cm, (b) 241 and 230 cm, (c) 168 and 187 cm, and (d) 94 and 100 cm.

Fig. 12(b)) could not be due to plasma source limitations and is caused by something else. Similarly, the deviations below the linear response at high bias potentials above 300 V in the I^2 versus V plots of Test 1 (Fig. 11) and Test 2 [Fig. 10(a)] cannot be a plasma source limitation. However, we are not able to conclusively rule out plasma source issues for the highest currents achieved in Fig. 12(d). Further tests will be required to resolve this question.

We have also considered the possibility of probe end effects affecting our model results, which assumed a perfectly cylindrical probe, even though all probes were many hundreds of λ_D long and we would expect sheath sizes to be not too large [32]. End effects are well known and are often modeled by an ideal cylinder for the main portion of the probe with an ideal spherical collector at the end, but the effective radius of the spherical collector is found to be much wider than the actual probe radius [33] and thus difficult to model easily. We have attempted to analyze the question of end effects by taking advantage of the fact that we have data sets for two different probe lengths, with roughly the same end effects for a given bias potential (providing proper scaling for plasma density and probe dimensions are considered). As a function of bias, we would expect end effects to be small at low bias potentials and vary with $V^{0.5}$ given that an infinite cylindrical probe would have a $V^{0.5}$ dependence with bias voltage and a spherical collector would have a corresponding $V^{1.0}$ relationship (electron temperature and plasma potential may also play a role). To do this analysis, we begin by defining the ratio of end-effect current to the undisturbed cylindrical probe current as either K_{10} or K_{30} for the 10- or 30-cm

probes, respectively (Test 1 and 2, respectively), and use as follows (here we assume the distances are exactly a factor of 3 different and densities are equal for simplicity):

$$I_{10} = I_{p10} + I_E = I_{p10}(1 + K_{10}) \quad (4)$$

and

$$\begin{aligned} I_{30} &= I_{p30} + I_E = I_{p30}(1 + K_{30}) \\ &= 3I_{p10} \left(1 + \frac{K_{10}}{3} \right) \end{aligned} \quad (5)$$

where I_{10} and I_{30} are the measured total currents for the two cases at a given bias potential, I_{pXX} is the portion of the total current from an ideal cylindrical probe response, and I_E is the end-effect current assumed to be the same for both probes. We define an additional parameter, $\beta = 3I_{10}/I_{30}$, which is the ratio of measured currents with an additional factor of 3 multiplying the 10-cm (Test 1) data. It is then possible to solve for K_{10} in terms of β using (4) and (5)

$$K_{10} = \frac{\beta - 1}{1 - \frac{\beta}{3}}. \quad (6)$$

The results of this analysis indicate that at the two farthest distances, K_{10} was on the order of 0.25 at a potential of 300 V, but at the next closest distance it has jumped to around 0.6. At the closest distance it even approaches a value of 1 (assuming there were no plasma source limitation). We do not find these results wholly satisfactory given that the I^2 versus V plots in Figs. 10 and 11 are linear in the higher voltages approaching 300 V and we would expect an end effect to be indicated by a nonlinear character above the straight-line fits in the figures for the tape

samples. We are thus left to remain concerned about end effects but not able to conclusively state their importance without further experiments. However, if this analysis is correct, then end effects should be smaller by about a factor of three for the Test 2 case. In future experiments, we plan to use electrical guards at each sample end to minimize end effects, although the mechanical complexity for these small probes would be considerable.

VI. FUTURE TESTS

We are preparing new experiments to help clarify and expand upon these initial results. First, as stated, we will be including guards to mitigate against end effects in all samples. We plan on more fully mapping and characterizing the plume and its energy distribution. We will be increasing the effective width of the tape samples to approximately $30\lambda_D$. We are also planning a series of tests with porous tape samples using holes and slots. The density and geometry of these holes and slots will be varied. It would be useful to determine if turbulent effects are present in the near plasma as the bias is increased beyond the incoming ion beam energy as was seen for TSS-1R. Different beam energies can be used. Magnetic field effects can also be tested.

VII. CONCLUSION

We believe that the experimental results to date in high-speed plasma indicate that the thin tape tether will be a viable option for bare-tether geometries. Widths well above a Debye length can be used and still closely obey the theoretical response developed for OML circular cylinder collectors in an unmagnetized stationary plasma. It appears that using a circular cylinder model of equal area to the thin tape provides close agreement up to some width. However, we are not able to say based on experiment what the maximum dimension can be but it is well beyond the $4\lambda_D$ maximum suggested by Sanmartín and Estes [30], though this was thought to be a weak constraint. What can be said is that the width can be at least $\sim 11\lambda_D$ and possibly wider. In fact, our Test 1 results even suggested as much as $\sim 19\lambda_D$, but additional experiments at these and larger widths where issues of end effects or questions of excessive current collection (exceeding plasma source availability) are not a concern will be required to establish a definitive limit.

Regardless of the similarities with OML theory for a stationary plasma, there definitely were differences. First, orienting the tape sample parallel or perpendicular to the plasma flow yielded a divergence in the current response above a bias potential that is near the estimated energy of the incoming beam ions regardless of plasma density. The perpendicular orientation consistently collected more current. The observed split in the two curves was generally more pronounced at larger effective widths (higher densities). We note the similarity to TSS-1R results, which also had a change in its current-voltage character as the satellite potential exceeded the ram kinetic energy of O^+ ions (5.3 eV). Specifically, TSS-1R data showed enhanced current collection as the bias approached and exceeded the ram kinetic energy, which was attributed to turbulence and plasma heating effects. Additional experiments of our simulated tape tethers may help us determine the cause of the difference in performance for different orientations.

Second, we also note that it was necessary to be above at least the same bias potential near the ion beam energy in order to

observe a $V^{0.5}$ current-voltage “saturated” character for either the reference cylinder or tape samples. We suggest that this is also a velocity effect not expected in a stationary plasma.

The possibility of end-effects cannot be ruled out even for our longer samples (Test 2), although we estimate that it represents less than a 10% increase in current at least at the farthest distance. In addition, current saturation due to plasma source limitations cannot be ruled out at closest distances for the long probe case (Test 2). None of these limitations significantly modify our general conclusions. In future experiments, a more sophisticated configuration will be used to minimize/eliminate these factors. We parenthetically note that adding an end collector could supplement current collection and be of some value in certain situations, as suggested in the literature [5], [7]–[10], [34].

ACKNOWLEDGMENT

The authors would like to thank J. Van Noord, T. Patrick, and the PEPL research group for assistance in performing these experiments. The authors also wish to thank Dr. D. Cooke, Dr. R. Estes, Dr. M. Martínez-Sánchez, Dr. J. Sanmartín, Dr. N. Stone, and Dr. K. Wright for useful discussions about these results and their interpretation.

REFERENCES

- [1] J. R. Sanmartín, M. Martínez-Sánchez, and E. Ahedo, “Bare wire anodes for electrodynamic tethers,” *J. Prop. Power*, vol. 9, no. 3, pp. 353–360, 1993.
- [2] N. H. Stone and C. Bonifazi, “The TSS-1R mission: Overview and scientific context,” *Geophysical Res. Lett.*, vol. 25, no. 4, pp. 409–412, 1998.
- [3] L. Johnson, R. D. Estes, E. Lorenzini, M. Martínez-Sánchez, and J. Sanmartín, “Propulsive small expendable deployer system experiment,” *J. Spacecraft Rockets*, vol. 37, no. 2, pp. 173–176, 2000.
- [4] J. Van Noord, B. West, and B. Gilchrist, “Electrodynamic tape tether performance with varying tether widths at low Earth altitudes,” in *39th Aerospace Sciences Meeting Exhibit*, Reno, NV, Jan. 8–11, 2001, AIAA Paper 2001-1141.
- [5] N. H. Stone and P. A. Gierow, “A preliminary assessment of passive end-body plasma contactors [for electrodynamic tether systems],” in *39th Aerospace Sciences Meeting Exhibit*, Reno, NV, Jan. 8–11, 2001, AIAA Paper 2001-1165.
- [6] M. Dobrowolny, G. Vannaroni, and F. De Venuto, “Electrodynamic de-orbiting of LEO satellites,” *Nuovo Cimento*, vol. 23C, no. 1, pp. 85–105, 2000.
- [7] M. Dobrowolny and F. Vannaroni, private communication, 1999.
- [8] R. D. Estes, J. Sanmartín, and M. Martínez-Sánchez, “Performance of bare-tether systems under varying magnetic and plasma conditions,” *J. Spacecraft Rockets*, vol. 37, no. 2, pp. 197–204, 2000.
- [9] E. Ahedo and J. Sanmartín, “Analysis of bare-tether systems for de-orbiting low-Earth-orbit satellites,” *J. Spacecraft Rockets*, vol. 39, no. 2, pp. 198–205, 2002.
- [10] J. R. Sanmartín, R. D. Estes, and E. C. Lorenzini, “Efficiency of different types of ED-tether thrusters,” in *Space Technol. Applicat. Int. Forum (STAIF-2001)*, Albuquerque, NM, Feb. 11–14, 2001.
- [11] L. Johnson, B. E. Gilchrist, R. D. Estes, E. Lorenzini, and J. Ballance, “Propulsive small expendable deployer system (ProSEDS) space experiment,” Paper AIAA-98-4035, 1998.
- [12] J. Van Noord and R. Strumfels, “Electrodynamic tether optimization for the STEP-AirSEDS mission,” in *37th Joint Prop. Conf.*, Salt Lake City, UT, July 8–11, 2001, Paper AIAA 2001-3980.
- [13] R. L. Forward, “Failsafe multistrand tether structures for space propulsion,” Paper AIAA-92-3214, 1992.
- [14] A. D. Gallimore, S.-W. Kim, J. E. Foster, L. B. King, and F. S. Gulczinski, III, “Near and far field plume studies of a one-kilowatt arcjet,” *AIAA J. Prop. Power*, vol. 12, pp. 105–111, 1996.
- [15] R. O. Jenkins and W. G. Trodden, *Electron and Ion Emission From Solids*. New York: Dover, 1965.
- [16] J. M. Haas, F. S. Gulczinski, III, A. D. Gallimore, G. G. Spanjers, and R. A. Spores, “Performance characteristics of a 5 kW laboratory Hall thruster,” Paper AIAA-98-3503, 1998.

- [17] G. Vannaroni and F. De Venuto, "Current collection by bare tether samples in a simulated ionospheric environment," Istituto di Fisica dello Spazio Interplanetario CNR, IFSI-2001-17, July 2001.
- [18] D. Keefer *et al.*, "Multiplexed laser induced fluorescence and nonequilibrium processes in arcjets," in *25th Plasmadynamics Lasers Conf.*, July 1992, Paper AIAA-94-2656.
- [19] G. J. Williams, Jr., T. B. Smith, F. S. Gulczinski, B. E. Beal, A. D. Gallimore, and R. P. Drake, "Laser induced fluorescence measurement of ion velocities in the plume of a Hall effect thruster," in *35th Joint Propulsion Conf.*, 1999, Paper AIAA-1999-2424.
- [20] G. J. Williams, Jr., "The use of laser-induced fluorescence to characterize discharge cathode erosion in a 30 cm ring-cusp ion thruster," Ph.D. dissertation, Dept. Aerospace Eng., The University of Michigan, Sept. 2000.
- [21] M. L. Walker, A. D. Gallimore, J. Koo, and I. Boyd, "Pressure map of a facility as a function of flow rates to study facility effects," Paper, AIAA-2002-3815, 2002.
- [22] S. H. Pullins, Y. Chiu, D. J. Levandier, and R. A. Dressler, "Ion dynamics in Hall effect and ion thrusters—Xe⁺ + Xe symmetric charge transfer," AIAA Paper 00-0603, 2000.
- [23] S. Miller, D. J. Levandier, Y. Chiu, and R. A. Dressler, "Xenon charge exchange cross sections for electrostatic thruster models," *J. Appl. Phys.*, vol. 91, pp. 984–991, 2002.
- [24] D. C. Thompson, C. Bonifazi, B. E. Gilchrist, S. D. Williams, W. J. Raitt, J.-P. Lebreton, W. J. Burke, N. H. Stone, and K. H. Wright, Jr., "The current–voltage characteristics of a large probe in low earth orbit: TSS-1R results," *Geophys. Res. Lett.*, vol. 25, no. 4, pp. 413–416, 1998.
- [25] I. Katz, E. Melchioni, M. Mandell, M. Oberhardt, D. Thompson, T. Neubert, B. Gilchrist, and C. Bonifazi, "Observations of ionosphere heating in the TSS-1 subsatellite presheath," *J. Geophys. Res.*, vol. 99, no. A5, pp. 8961–8969, 1993.
- [26] L. Iess, C. Harvey, G. Vannaroni, J. P. Lebreton, M. Dobrowolny, R. Manning, P. Cerulli-Irelli, A. Onelli, and F. De Venuto, "Plasma waves in the sheath of the TSS-1R satellite," *Geophys. Res. Lett.*, vol. 25, no. 4, pp. 421–424, 1998.
- [27] J. D. Winningham, N. H. Stone, C. A. Gurgiolo, K. H. Wright, R. A. Frahm, and C. A. Bonifazi, "Suprathermal electrons observed on the TSS-1R satellite," *Geophys. Res. Lett.*, vol. 25, no. 4, pp. 429–432, 1998.
- [28] M. Dobrowolny, U. Guidoni, E. Melchioni, C. Vannaroni, and J. P. Lebreton, "Current–voltage characteristics of the TSS-1 satellite," *J. Geophys. Res.*, vol. 100, no. A12, pp. 23 953–23 957, 1995.
- [29] M. Kruijff, E. J. van der Heide, F. De Venuto, M. Dobrowolny, and G. Vannaroni, "Long term stability of bare conductive tethers: Combined results from plasma chamber tests and advanced simulations," in *2001 Space Technologies and Applications Int. Forum*, 2001.
- [30] J. R. Sanmartín and R. D. Estes, "The orbital-motion-limited regime of cylindrical langmuir probes," *Phys. Plasmas*, vol. 6, no. 1, pp. 395–405, 1999.
- [31] —, "Interference of parallel cylindrical Langmuir probes," *Phys. Plasmas*, vol. 8, no. 9, pp. 4234–4239, 2001.
- [32] R. D. Estes and J. R. Sanmartín, "Cylindrical Langmuir probes beyond the orbital-motion-limited regime," *Phys. Plasmas*, vol. 7, no. 10, pp. 4320–4325, 2000.
- [33] D. Johannig, W. Seifert, and A. Best, "Analytic density correction for cylindrical Langmuir probes showing end effects," *Plasma Physics Controlled Fusion*, vol. 27, no. 2, pp. 159–179, 1985.
- [34] J. R. Sanmartín, R. D. Estes, and E. C. Lorenzini, "Efficiency of different types of ED-tether thrusters," in *Proc. Amer. Inst. Phys. (A01-45 105 12-12)*, Melville, NY, 2001, (AIP Conf. Proc., no. 552), pp. 479–487.



Brian E. Gilchrist (S'75–M'78) received the B.S. and M.S. degrees from the University of Illinois, Urbana, in 1977 and 1979, respectively, and the Ph.D. degree from Stanford University, Stanford, CA, in 1991, all in electrical engineering.

He had 12 years of industrial microwave systems and technology research and development experience prior to receiving the Ph.D. degree. His research interests include developing electrodynamic tethers as a new propellantless space propulsion technology, plasma diagnostics for the ionosphere

and for plasma electric propulsion systems, and spacecraft technology. Since 1997, he has been an Associate Professor of electrical engineering and space science at the University of Michigan, Ann Arbor. He is also a member of the Radiation and Space Physics Research Laboratories.



Sven G. Bilén (S'90–M'98) received the B.S. degree from The Pennsylvania State University in 1991 and the M.S.E. and Ph.D. degrees from the University of Michigan, Ann Arbor, in 1993 and 1998, respectively.

In January 2000, he joined The Pennsylvania State University as an Assistant Professor in electrical engineering and in engineering design. His work at the University of Michigan examined the general propagation behavior of high-voltage EM pulses along conductors in low-density cold plasmas with the specific application of electrodynamic tethers in the ionosphere. His research interests currently include electrodynamic-tether science, technology, and applications; *in situ* measurements of space plasmas and environments; circuit modeling of plasmas and spacecraft–plasma interactions; and plasma diagnostics for space plasmas, plasma electric thrusters, and semiconductor plasma processing.

Dr. Bilén is a member of AIAA, AGU, ASEE, and Sigma Xi.



Éric Choinière (S'98) received the B.Eng. and M.S. degrees in electrical engineering from École Polytechnique de Montréal, Canada, in 1997 and 1999, respectively.

He is currently working toward the Ph.D. degree in electrical engineering at the University of Michigan and is affiliated with the Radiation Laboratory and the Space Electrodynamics and Tether Systems Group. The research work that led to his M.S. thesis involved the development of a computational model for multilayered printed array antennas and frequency selective surfaces. His current research includes both the experimental testing and computational modeling of the electron collection processes to bare electrodynamic space tethers.

Dr. Choinière is a member of the Applied Computational Electromagnetics Society, the Microwave Theory and Techniques Society, and the Nuclear and Plasma Science Society.



Alec D. Gallimore received the B.S. degree in aeronautical engineering from Rensselaer Polytechnic Institute, Troy, NY, in 1986, and the M.A. and Ph.D. degrees in aerospace engineering from Princeton University, Princeton, NJ, in 1988 and 1992, respectively.

He is an Associate Professor of aerospace engineering and applied physics at the University of Michigan, Ann Arbor, where he directs the Plasmadynamics and Electric Propulsion Laboratory. His primary research interests include electric propulsion, plasma diagnostics, space plasma simulation, and electrode physics. He has experience with a wide array of electric propulsion technologies, including MPD thrusters, arcjets, ion engines, and Hall thrusters, and he has implemented a variety of probe, microwave, and optical plasma diagnostics.



Timothy B. Smith received the B.S. degree in aerospace engineering from the University of Virginia, in 1987, the M.S. degree in ocean engineering from George Washington University, in 1996, and M.S.E. degrees in aerospace and nuclear engineering from the University of Michigan, Ann Arbor, in 1998.

He is a graduate student Research Assistant in the Aerospace Engineering Department of the University of Michigan, carrying out research at the Plasmadynamics and Electric Propulsion Laboratory (PEPL).

His primary research interests include electric propulsion, optical plasma diagnostics, and deconvolution methods. He has experience with Hall thrusters, ion engines, and marine propulsors, and has co-authored 18 articles on electric propulsion, experimental astrophysics, and naval architecture. He has worked for the U.S. Air Force, the University of Virginia, Douglas Aircraft, and the Naval Surface Warfare Center, Carderock Division.